INTERNATIONAL JOURNAL FOR NUMERICAL METHODS IN FLUIDS
Int. J. Numer. Meth. Fluids 2009; **61**:536–551
Published online 1 December 2008 in Wiley InterScience (www.interscience.wiley.com). DOI: 10.1002/fld.1963

Numerical study on heavy rigid particle motion in a plane wake flow by spectral element method

Zuo-Bing Wu*, †

State Key Laboratory of Nonlinear Mechanics, Institute of Mechanics, Chinese Academy of Sciences, Beijing 100190, China

SUMMARY

Experimental particle dispersion patterns in a plane wake flow at a high Reynolds number have been predicted numerically by discrete vortex method (*Phys. Fluids A* 1992; **4**:2244–2251; *Int. J. Multiphase Flow* 2000; **26**:1583–1607). To address the particle motion at a moderate Reynolds number, spectral element method is employed to provide an instantaneous wake flow field for particle dynamics equations, which are solved to make a detail classification of the patterns in relation to the Stokes and Froude numbers. It is found that particle motion features only depend on the Stokes number at a high Froude number and depend on both numbers at a low Froude number. A ratio of the Stokes number to squared Froude number is introduced and threshold values of this parameter are evaluated that delineate the different regions of particle behavior. The parameter describes approximately the gravitational settling velocity divided by the characteristic velocity of wake flow. In order to present effects of particle density but preserve rigid sphere, hollow sphere particle dynamics in the plane wake flow is investigated. The evolution of hollow particle motion patterns for the increase of equivalent particle density corresponds to that of solid particle motion patterns for the decrease of particle size. Although the thresholds change a little, the parameter can still make a good qualitative classification of particle motion patterns as the inner diameter changes. Copyright © 2008 John Wiley & Sons, Ltd.

Received 4 September 2007; Revised 5 October 2008; Accepted 8 October 2008

KEY WORDS: spectral element method; plane wake flow; heavy rigid particle motion features; two-phase flows

1. INTRODUCTION

The motion of particles in a nonuniform flow has wide technological applications, such as to increase combustion efficiency and forecast environmental pollution [1, 2]. To understand flow mechanism, some theoretical models and computational methods are developed in the particulate

*Correspondence to: Zuo-Bing Wu, State Key Laboratory of Nonlinear Mechanics, Institute of Mechanics, Chinese Academy of Sciences, Beijing 100190, China.
†E-mail: wuzb@lnm.imech.ac.cn, z_b_wu@hotmail.com

two-phase flow research. Owing to particle motion in the low Reynolds number category, the motion equation for a small rigid sphere in a nonuniform flow field is proposed [3, 4]. Related studies show that even when the background flow fields are very simple, the motion can have abundant phenomena: suspended particles accumulate along simple isolated curves for a cellular flow field [5] and periodic, quasiperiodic or chaotic trajectories for a periodic Stuart vortex flow [6]. In particular, for a von Kármán vortex flow field, the suspended particle trajectories are determined as chaotic by calculating the maximal Lyapunov exponent [7]. A route of bifurcation process to a chaotic trajectory and more attractors in a bifurcation diagram related to particle parameters are reported [8].

In both a plane mixing layer and wake flow, influences of large-scale vortices on the particle dispersion process are observed experimentally and simulated by discrete vortex method [9]. In a plane mixing layer, the particles are found to concentrate near the outer edges of the vortex structures. It can be described by the particle sheet stretching and folding mechanisms in vortex pairing interactions [10]. For the particle dispersion in a plane wake flow at a high Reynolds number (10^4), highly organized patterns of particle concentrations are produced in a correlation with the Stokes number. The particles at intermediate Stokes number are focused into sheet-like regions near the boundaries of the large-scale vortex structures [11, 12].

To investigate numerically the particle trajectories in the plane wake flow behind a circular cylinder at a moderate Reynolds number (10^2), Navier–Stokes equations will be solved by direct numerical simulation method. In the direct numerical simulation for the Navier–Stokes equations, high-order splitting schemes [13] and spectral element method [14–16], which combine accuracy in time and space and flexibility in geometry, provide a very efficient algorithm. The combined algorithm has been employed successfully in studying nonlinear dynamics and transition to turbulence in the wake of a circular cylinder [17, 18]. In this paper, we will consider the solid and hollow particle dynamics in a plane wake flow behind a circular cylinder at $Re=100$ and make a detail classification of the patterns in relation to the Stokes and Froude numbers.

2. GOVERNING EQUATIONS

The motion of a small hollow spherical particle in a nonuniform flow field $\mathbf{u}$ is governed by the momentum equation [3, 4, 6]

$$\begin{aligned}\frac{\pi}{6}d_{\mathrm{p}}^3(1-\xi^3)(\rho_{\mathrm{p}}+0.5\rho_{\mathrm{f}})\frac{\mathrm{d}\mathbf{V}}{\mathrm{d}t} &= \frac{\pi}{6}d_{\mathrm{p}}^3(1-\xi^3)(\rho_{\mathrm{p}}-\rho_{\mathrm{f}})\mathbf{g}+\frac{\pi}{4}d_{\mathrm{p}}^3(1-\xi^3)\rho_{\mathrm{f}}\frac{\mathrm{D}\mathbf{u}}{\mathrm{D}t}\\ &\quad +3\pi d_{\mathrm{p}}\nu_{\mathrm{f}}\rho_{\mathrm{f}}(\mathbf{u}-\mathbf{V})f_d+\frac{3}{2}(\pi\nu_{\mathrm{f}})^{1/2}d_{\mathrm{p}}^2\rho_{\mathrm{f}}\\ &\quad \times\int_0^t\frac{1}{\sqrt{t-\tau}}\left(\frac{\mathrm{d}\mathbf{u}}{\mathrm{d}\tau}-\frac{\mathrm{d}\mathbf{V}}{\mathrm{d}\tau}\right)\mathrm{d}\tau\\ &\quad +\frac{\pi}{12}d_{\mathrm{p}}^3(1-\xi^3)\rho_{\mathrm{f}}(\mathbf{u}-\mathbf{V})\times\omega_z\mathbf{k}\end{aligned} \tag{1}$$

DOI: 10.1002/fld

where $\xi = d_v/d_\mathrm{p}$ is a ratio of inner diameter d_v of the particle to outer diameter d_p, $\mathbf{V}$ is the velocity of the particle, ρ is the density, $\mathbf{g}$ is the gravitational acceleration, ν_f is the fluid kinematic viscosity, ω_z is the vorticity of the flow fluid and the subscripts f and p refer to the fluid and particle, respectively. $\rho_\mathrm{p}/(1-\xi^3)$ reflects an equivalent particle density. The derivatives $\mathrm{D}/\mathrm{D}t$ and $\mathrm{d}/\mathrm{d}t$ are used to denote a time derivative following a fluid element and the moving sphere, respectively. The parameter f_d relating to the Reynolds number of the particle

$$\left(Re_\mathrm{p} = \frac{|\mathbf{u}-\mathbf{V}|d_\mathrm{p}}{\nu_\mathrm{f}} \right)$$

is described [19] as

$$f_d = 1 + 0.1315 Re_\mathrm{p}^{0.82-0.05 log_{10}^{Re_\mathrm{p}}}, \quad 0.01 < Re_\mathrm{p} \leqslant 20 \tag{2}$$

Introducing the dimensionless quantities $\delta = \rho_\mathrm{p}/\rho_\mathrm{f}(1-\xi^3), \varepsilon = 1/(0.5+\delta), \mathbf{x}^* = \mathbf{x}/L, t^* = t/(L/U_\infty), \mathbf{u}^* = \mathbf{u}/U_\infty, \mathbf{V}^* = \mathbf{V}/U_\infty$ and $\mathbf{g}^* = \mathbf{g}/g$, we nondimensionlize Equation (1) and describe as follows:

$$\begin{aligned} \frac{\mathrm{d}\mathbf{V}}{\mathrm{d}t} = {} & \frac{(1-1.5\varepsilon)}{Fr^2}\mathbf{g} + \frac{3\varepsilon}{2}\frac{\mathrm{D}\mathbf{u}}{\mathrm{D}t} + \frac{f_d}{St}(\mathbf{u}-\mathbf{V}) \\ & + 3\sqrt{\frac{\varepsilon}{2\pi St}} \int_0^t \frac{1}{\sqrt{t-\tau}} \left(\frac{\mathrm{d}\mathbf{u}}{\mathrm{d}\tau} - \frac{\mathrm{d}\mathbf{V}}{\mathrm{d}\tau} \right) \mathrm{d}\tau + \frac{\varepsilon}{2}(\mathbf{u}-\mathbf{V}) \times \omega_z \mathbf{k} \end{aligned} \tag{3}$$

where the Froude number $Fr = U_\infty/\sqrt{gL}$ (U_∞ and L are the free-stream velocity and the diameter of circular cylinder, respectively), the Stokes number $St = U_\infty T/L$ (T is the particle viscous relaxation time $d_\mathrm{p}^2/18\varepsilon\nu_\mathrm{f}$) and the asterisks '$*$' for the dimensionless quantities are omitted for convenience. Moreover, the Reynolds number of the particle is written as $Re_\mathrm{p} = \Re_\mathrm{p}|\mathbf{u}-\mathbf{V}|$ ($\Re_\mathrm{p} = U_\infty d_\mathrm{p}/\nu_\mathrm{f}$).

The flow field $\mathbf{u}$ is chosen as a plane wake flow. The incompressible plane wake flow is governed by the Navier–Stokes equations in the form

$$\begin{aligned} & \nabla \cdot \mathbf{u} = 0 \quad \text{in } \Omega \\ & \frac{\partial \mathbf{u}}{\partial t} = -\nabla p + N(\mathbf{u}) + \frac{1}{Re} L(\mathbf{u}) \quad \text{in } \Omega \end{aligned} \tag{4}$$

subject to boundary condition of the form

$$\mathbf{u} = \mathbf{u}^0 \quad \text{on } \Gamma \tag{5}$$

where $\mathbf{u}$ is the fluid velocity and p is the fluid pressure divided by fluid density. The parameter $Re = U_\infty L/\nu_\mathrm{f}$ is the Reynolds number of the plane wake flow. The linear diffusion and nonlinear advection terms are described by

$$\begin{aligned} L(\mathbf{u}) &= \nabla^2 \mathbf{u} \\ N(\mathbf{u}) &= -\tfrac{1}{2}[\mathbf{u} \cdot \nabla \mathbf{u} + \nabla \cdot \mathbf{u}\mathbf{u}] \end{aligned} \tag{6}$$

where $N(\mathbf{u})$ is written in a skew-symmetric form to minimize aliasing errors [20].

DOI: 10.1002/fld

As air is chosen as the fluid media in the flow, the properties of fluid in Equation (3) are described as $\rho_f = 1.225\,\mathrm{kg/m^3}$ and $v_f = 1.45\times10^{-5}\,\mathrm{m^2/s}$ [21]. The free-stream velocity is taken as $U_\infty = O(1)\,\mathrm{m/s}$. The particle density is kept as $\rho_p = 2.4\times10^3\,\mathrm{kg/m^3}$ from [11]. In order to understand the dilute particle dynamics, we analyze orders of magnitude of parameters in Equation (3). For giving physical coefficients in the calculation, the parameters f_d and Fr^2 appear to be on the order 1 and 10^2.

(1) *For solid sphere* ($\xi = 0$): Since the δ is fixed as the order 10^3, the parameter ε appears to be on the order 10^{-3}. When d_p is taken as the order 10^{-6}–$10^{-4}\,\mathrm{m}$, the parameters T and St appear to be on the order 10^{-5}–$10^{-1}\,\mathrm{s}$ and 10^{-2}–10^2, respectively. In this case, the stress tensor term of fluid $(3\varepsilon/2)\mathrm{D}\mathbf{u}/\mathrm{D}t$, the Basset history term

$$3\sqrt{\frac{\varepsilon}{2\pi St}}\int_0^t \frac{1}{\sqrt{t-\tau}}\left(\frac{\mathrm{d}\mathbf{u}}{\mathrm{d}\tau}-\frac{\mathrm{d}\mathbf{V}}{\mathrm{d}\tau}\right)\mathrm{d}\tau$$

and lift force term $\varepsilon/2(\mathbf{u}-\mathbf{V})\times\omega_z\mathbf{k}$ has smaller orders than the drag term $f_d/St(\mathbf{u}-\mathbf{V})$ and gravity term $(1-1.5\varepsilon)/Fr^2\mathbf{g}$ in Equation (3). Thus, Equation (3) is dominated by the drag term and gravity term. The particle motion is described by a four-dimensional dynamical system of the form

$$\begin{aligned}\frac{\mathrm{d}\mathbf{r}}{\mathrm{d}t} &= \mathbf{V}\\ \frac{\mathrm{d}\mathbf{V}}{\mathrm{d}t} &= \frac{1-1.5\varepsilon}{Fr^2}\mathbf{g}+\frac{f_d}{St}(\mathbf{u}-\mathbf{V})\end{aligned} \tag{7}$$

(2) *For hollow sphere* ($1>\xi>0$): Since the δ can be changed in a range of $0-O(10^3)$, the parameter ε appears to be in the range $2-O(10^{-3})$. When the particle outer diameter d_p is fixed as $O(10^{-5})\,\mathrm{m}$, the parameters T and St appear to be on the order 10^{-6}–$10^{-3}\,\mathrm{s}$ and 10^{-1}–10^2, respectively. In this case, we only reduce the Basset history term and keep other four terms in Equation (3). The particle motion is described by a four-dimensional dynamical system of the form

$$\begin{aligned}\frac{\mathrm{d}\mathbf{r}}{\mathrm{d}t} &= \mathbf{V}\\ \frac{\mathrm{d}\mathbf{V}}{\mathrm{d}t} &= \frac{(1-1.5\varepsilon)}{Fr^2}\mathbf{g}+\frac{3\varepsilon}{2}\frac{\mathrm{D}\mathbf{u}}{\mathrm{D}t}+\frac{f_d}{St}(\mathbf{u}-\mathbf{V})+\frac{\varepsilon}{2}(\mathbf{u}-\mathbf{V})\times\omega_z\mathbf{k}\end{aligned} \tag{8}$$

3. NUMERICAL METHODS

In the particle dynamical equations, instantaneous flow field $\mathbf{u}(\mathbf{x}^n, t^n)$ is provided by solving Navier–Stokes equation (4). The time discretization of the Navier–Stokes equations employs a

DOI: 10.1002/fld

high-order splitting algorithm. The semi-discrete formulation [13] is written as

$$\begin{aligned}\frac{\hat{\mathbf{u}}-\sum_{q=0}^{J-1}\alpha_q\mathbf{u}^{n-q}}{\Delta t}&=\sum_{q=0}^{J-1}\beta_q N(\mathbf{u}^{n-q})\\ \frac{\hat{\hat{\mathbf{u}}}-\hat{\mathbf{u}}}{\Delta t}&=-\nabla p^{n+1},\quad \nabla\cdot\hat{\hat{\mathbf{u}}}=0\\ \frac{\gamma_0\mathbf{u}^{n+1}-\hat{\hat{\mathbf{u}}}}{\Delta t}&=\frac{1}{Re}L(\mathbf{u}^{n+1})\end{aligned}\tag{9}$$

Here $\hat{\mathbf{u}}, \hat{\hat{\mathbf{u}}}$ are intermediate velocity fields and the constants α_q, β_q and γ_0 are integration coefficients for a mixed explicit/implicit stiffly stable scheme of order $J=3$. In this calculation, the parameters $\alpha_q(q=1,2,3), \beta_q(q=1,2,3)$ and γ_0 are chosen as $(3,-\frac{3}{2},\frac{1}{3}), (3,-3,1), \frac{11}{6}$, respectively. The boundary condition for the pressure is given by

$$\frac{\partial p^{n+1}}{\partial n}=-\mathbf{n}\cdot\left[\sum_{q=0}^{J-1}\beta_q N(\mathbf{u}^{n-q})-\frac{1}{Re}\sum_{q=0}^{J-1}\beta_q\nabla\times(\nabla\times\mathbf{u}^{n-q})\right]\tag{10}$$

where $\mathbf{n}$ is a normal vector to the boundary. The advantage of this scheme is that the stability properties remain almost constant as the accuracy of the integration increases.

The spatial discretization of Equation (9) is obtained by using the spectral element method [14–16]. The spatial discretization proceeds by first covering the domain Ω with general quadrangles. Each quadrangle is mapped from the physical space (x, y) into the local co-ordinate system (r, s) by an isoparametric tensor-product mapping

$$(x,y)_N^k=\sum_{i=0}^{N}\sum_{j=0}^{N}(X,Y)_{ij}^k h_i(r)h_j(s)\tag{11}$$

where $h_i(r)$ are the Nth-order local Lagrange interpolants and defined as $h_i(r_j)=\delta_{ij}$. δ_{ij} is the Kronecker-delta symbol. For the physical mesh $(X,Y)_{ij}^k$, we first specify their elemental boundary nodes according to a Chebyshev distribution in arclength. Then, we determine their internal elemental nodes from the elemental boundary nodes by an algebraic mapping [22, 23]

$$\begin{aligned}\Psi(r,s)=&\frac{1-s}{2}\pi_1(r)+\frac{1+s}{2}\pi_3(r)+\frac{1-r}{2}\left[\pi_2(s)-\frac{1+s}{2}\pi_2(1)-\frac{1-s}{2}\pi_2(-1)\right]\\ &+\frac{1+r}{2}\left[\pi_4(s)-\frac{1+s}{2}\pi_4(1)-\frac{1-s}{2}\pi_4(-1)\right]\end{aligned}\tag{12}$$

where $\pi_i(i=1,2,3,4)$ is a mapping from the four quadrilateral $\widehat{\Gamma}_i$ to Γ_i. For the r_i, we choose the Gauss–Lobatto Chebyshev points $r_i=-\cos\pi i/N$. The interpolants $h_i(r)$ can be written as

$$\begin{aligned}h_i(r)&=\mu_{ij}T(r)\\ \mu_{ij}&=\frac{2}{N}\frac{1}{\bar{c}_i\bar{c}_j}T_j(r_i)\end{aligned}\tag{13}$$

DOI: 10.1002/fld

Here the T_i are the Chebyshev polynomials $T_i(\cos\theta)=\cos i\theta$ and

$$\begin{aligned}\bar{c}_i &= 1 \quad \text{if } i\neq 0, N\\ \bar{c}_i &= 2 \quad \text{if } i=0, N\end{aligned} \tag{14}$$

In each isoparametric element, the velocity and pressure are interpolated in the same manner, that is,

$$(\mathbf{u}, p)_N^k=\sum_{i=0}^{N}\sum_{j=0}^{N}(\mathbf{U}, P)_{ij}^k h_i(r)h_j(s) \tag{15}$$

Thus, the first equation in Equation (9) is an explicit scheme, so that $\hat{\mathbf{u}}$ can be obtained immediately. As the second and third equations in Equation (9) are implicit schemes, two-dimensional Helmholtz equations can be deduced. Using the spectral element methods for the Helmholtz equations, we obtain linear equation groups. To solve the linear equation groups, we apply the standard static condensation technique for the total stiffness matrix, and the classical conjugate gradient method to get the solutions $\mathbf{u}^n$ [24, 25].

When the flow field $\mathbf{u}(\mathbf{x}^n, t^n)$ at the point $\mathbf{x}^n=(x, y)$ is obtained, we use a fourth-order Runge–Kutta algorithm to integrate Equation (7) for solid sphere motion and Equation (8) for hollow sphere motion with a time size τ. In the fourth-order Runge–Kutta algorithm, solutions of the equations are determined with flow fields at times t^n and $t^n+\tau/2$. Hence, the time size Δt for solving the Navier–Stokes equations is a half of τ. For a given point in the flow field $\mathbf{x}_n$, its position and corresponding physical quantities in element k can be determined by the algebraic mapping (12) and the isoparametric tensor-product mapping (15), respectively.

4. RESULTS

The calculation parameters used are: the element number is 116, the order of interpolation function is $N=8$, the streamwise length is 38 and the transverse width is 11. A spectral element mesh is shown in Figure 1. Boundary conditions required for the velocity field are: at the surface of the cylinder the fluid velocity satisfies the nonslip condition: $\mathbf{u}=(0, 0)$. Far away from the cylinder and outside the wake, it matches the free-stream velocity $\mathbf{u}=(1, 0)$ along the left boundary and $\partial u_x/\partial n=0, u_y=0$ along the upper and lower boundaries. The right boundary condition across downstream is $\partial\mathbf{u}(x, t)/\partial x=(0, 0)$ for the velocity and $p=0$ for pressure [26]. Boundary conditions for the pressure field, other than above one, require to satisfy the high-order Neumann boundary condition (10). The background flow field is obtained by integrating Equation (9) up to total time $t=270$ with a time size $\Delta t=0.01$.

Figure 2(a) displays instantaneous streamlines of the wake flow field behind a circular cylinder. A wave structure is developed in the wake along with time. The correspondent contour plot of vorticity is drawn in Figure 2(b). A regular von Kármán vortex street flow field appears in the wake, where pairs of vortices with different signs appear. The drag coefficient C_d is determined as 1.5, which is close to a previous calculation [27, 28].

From three points near the circular cylinder, particle injection rates in the x direction are kept at a low value of 0.01 m/s to reduce the wake-flow particle coupling. Using a fourth-order Runge–Kutta algorithm, we integrate Equation (7) for solid sphere and Equation (8) for hollow sphere with a time size $\tau=2\Delta t$, where Δt is 0.002. At each time step 20τ, a particle is injected into the flow field. In order to avoid complex treatment for the interaction between particles and the

DOI: 10.1002/fld

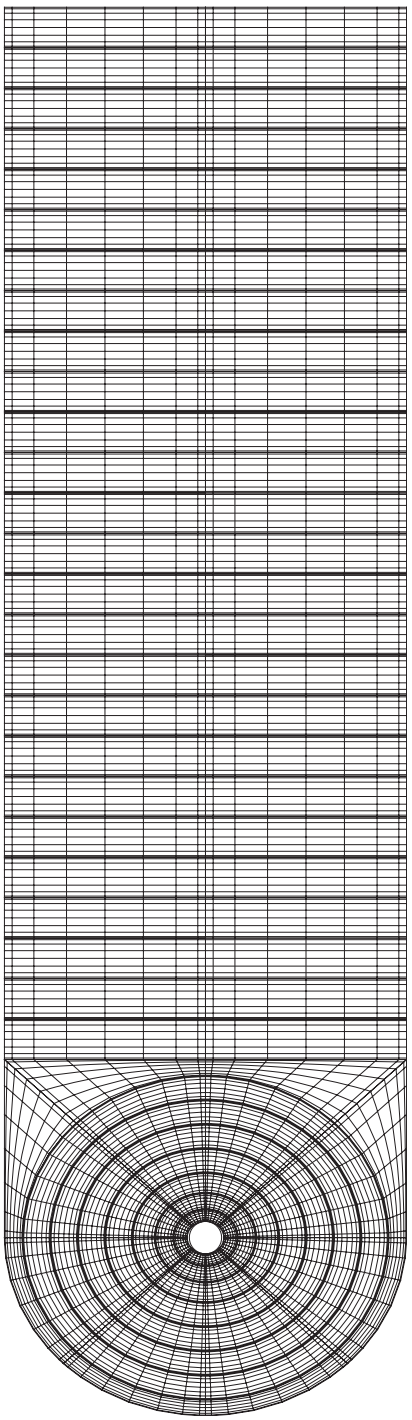

Figure 1. A spectral element mesh with eighth-order local Lagrange interpolates.

DOI: 10.1002/fld

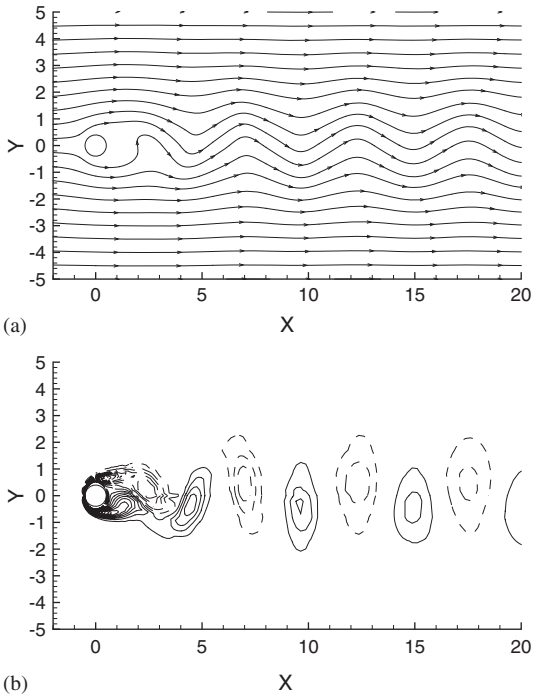

Figure 2. (a) Instantaneous streamlines and (b) vorticity counter plot for the plane wake flow at $Re=100$. Positive and negative vorticities are denoted by solid and dash lines, respectively.

circular cylinder, we take a numerical boundary $r_0=0.6$ for the particles. When a particle moves into the boundary, a repelling potential $1/r$ will be added to the particle. At the same time, in order to reduce effects of repelling potential on particle inertia, absolute values of velocity are fixed at 0.01 in the numerical boundary region. For some parameters of particles, Δt and r_0 will decrease and increase, respectively, so that particles can be always separated from the circular cylinder.

To quantify features of particle trajectories in the wake, we divide the range 4–20 in the streamwise direction for the intermediate and far wake flow field by 100. Particle number density in a strip $[x_i, x_i+\Delta x)$ is defined as

$$\rho^m_{x_i+\Delta x/2}=\frac{m_{x_i,x_i+\Delta x}}{M} \tag{16}$$

where $m_{x_i,x_i+\Delta x}$ is the particle number in the strip and M is the total number of particles in the range 4–20. Meanwhile, average relative velocity of $\mathbf{V}$ to $\mathbf{u}$ in the strip is defined as

$$v^m_{x_i+\Delta x/2}=\frac{\sum_{j=1}^{m_{x_i,x_i+\Delta x}}\sqrt{(V_{jx}-u_{jx})^2+(V_{jy}-u_{jy})^2}}{m_{x_i,x_i+\Delta x}} \tag{17}$$

In special, if $m_{x_i,x_i+\Delta x}$ is zero in the strip, $v^m_{x_i+\Delta x/2}$ is defined as zero.

(1) *For solid sphere*: In Equation (7), St affects the particle motion in both the x and y directions. However, Fr can only make changes of particle motion in the y direction. A different combination

DOI: 10.1002/fld

of St and Fr determines the particle motion in the plane wake flow. For a given Re, the Stokes and Froude numbers can be deduced as follows:

$$St = \frac{U_\infty^2 d_\mathrm{p}^2}{18\varepsilon v_\mathrm{f}^2 Re} \tag{18}$$

and

$$Fr^2 = \frac{U_\infty^3}{g v_\mathrm{f} Re} \tag{19}$$

First, we investigate the effects of St on the particle motion at a fixed Fr. As U_∞ is taken as 1 m/s, Fr^2 is fixed at 70.3 in Equation (19). As the increase in particle size or the Stokes number in Equation (18), organized structures of particles in the interaction with von Kármán vortex street are evaluated. Some basic features of particle trajectories are drawn in Figure 3. The particles follow the von Kármán vortex street downstream and interact with the vortices. For d_p in the range 1×10^{-6}–3×10^{-6} m ($St = 5.2\times10^{-3}$–4.7×10^{-2}), the particles mainly fill the cores of vortices as drawn in Figure 3(a). For d_p in the range 5×10^{-6}–8×10^{-6} m ($St = 0.13$–0.33), the particles move from the cores of vortices to outside of the cores as drawn in Figure 3(b)–(c). For d_p in the range 1×10^{-5}–2×10^{-5} m ($St = 0.52$–2.1), the particles concentrate at the edge of vortex street as drawn in Figure 3(d). For d_p in the range 3×10^{-5}–4×10^{-5} m ($St = 4.7$–8.3), the particles, which concentrate at the edge of vortex street, have a main distribution in the lower region as drawn in Figure 3(e). For d_p in the range 5×10^{-5}–7×10^{-5} m ($St = 12.9$–24.3), the particles escape from the vortex street central region as drawn in Figure 3(f). Thus, at a fixed Fr, the particle motion features change from a centralized distribution to a global distribution in the vortex street central region as St increases. Then, the solid particles accompany the vortices to move downstream and have larger transverse velocities than the fluid elements. In final, the transverse velocities of particles are large enough, so that they escape from the vortex street central region.

The above basic features of particle trajectories can be further quantitatively represented by the particle number density $\rho^m_{x_i+\Delta x/2}$ and average relative velocity $v^m_{x_i+\Delta x/2}$. For $St = 5.2\times10^{-3}$, in Figure 4(a), $\rho^m_{x_i+\Delta x/2}$ has several high values with a constant downstream distance. The constant distance presents the streamwise distance of two nearby vortices in the von Kármán vortex street. In Figure 4(b), $v^m_{x_i+\Delta x/2}$ is almost zero in the intermediate and far wake field. It is shown that the solid particle motion may display the fluid element one on both positions and velocities. For larger $St = 0.13$, 0.33 and 1.2, $\rho^m_{x_i+\Delta x/2}$ has only several high values with the constant distance in the intermediate wake field, but has not in the far wake field. Meanwhile, $v^m_{x_i+\Delta x/2}$ increases monotonously. It is shown that the solid particle velocities deviate from the fluid element ones. So, the solid particles may display the features of vortices in the intermediate wake, but have different velocities from fluid element ones. For large enough St ($St = 8.3$ and 18.6), $\rho^m_{x_i+\Delta x/2}$ has only finite values in the intermediate wake field, but has not regular characters. $v^m_{x_i+\Delta x/2}$ has very large values. It is shown that the solid particle motion deviates seriously from the fluid element one on both positions and velocities.

Second, we investigate effects of Fr on the particle motion at fixed St and Re. As Fr only depends on U_∞ in Equation (19), to preserve a fixed St in Equation (18), d_p will be changed in

DOI: 10.1002/fld

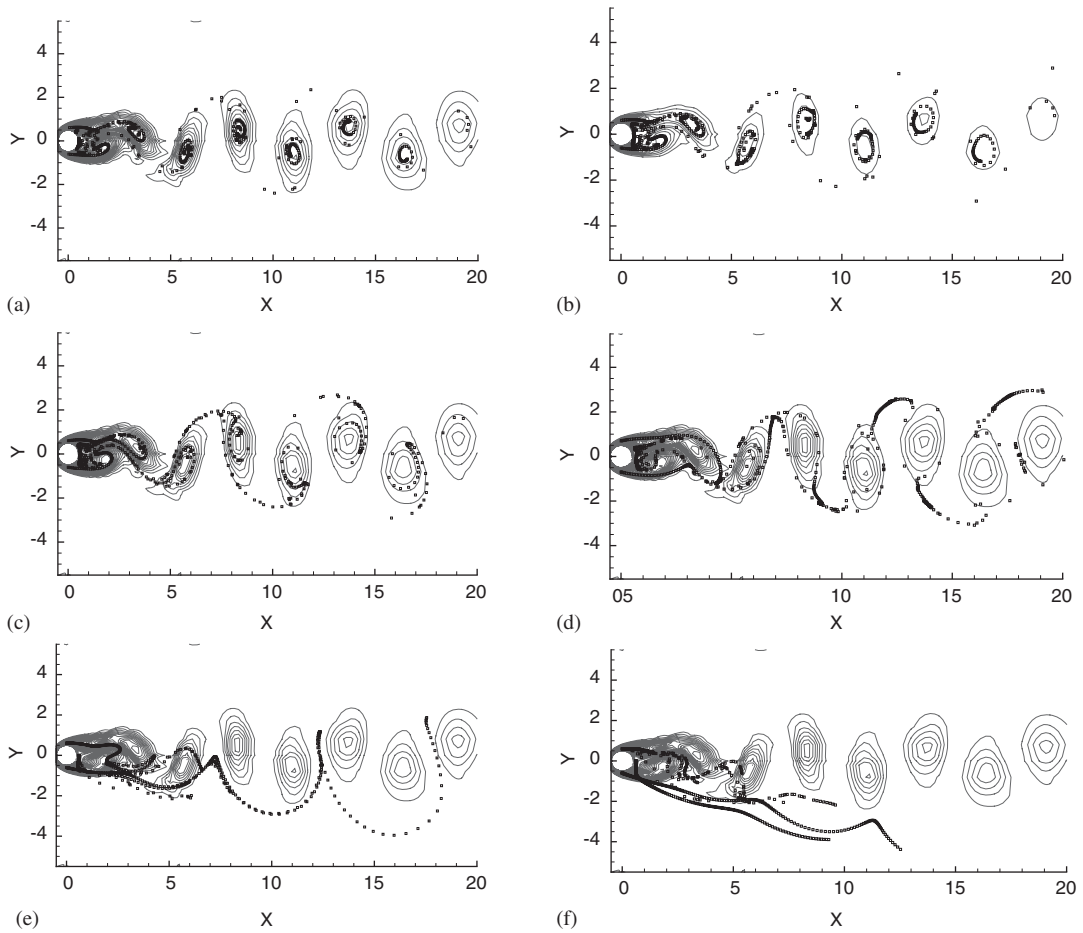

Figure 3. Instantaneous solid particle distribution and vorticity counter plot in the plane wake flow with a different particle size (Stokes number) and a fixed $Fr^2=70.3$: (a) $d_p=1\times10^{-6}$ m ($St=5.2\times10^{-3}$); (b) $d_p=5\times10^{-6}$ m (St=0.13); (c) $d_p=8\times10^{-6}$ m (St=0.33); (d) $d_p=1.5\times10^{-5}$ m (St=1.2); (e) $d_p=4\times10^{-5}$ m ($St=8.3$); and (f) $d_p=7\times10^{-5}$ m ($St=18.6$).

the fluctuation of U_∞. At the same time, to keep Re of the plane wake flow as a constant, L (the diameter of circular cylinder) will be changed in the fluctuation of U_∞. As we are only interested in the non-dimensional equations (3)(4), the variation of L is not reflected in the following analysis. For the fixed $St=0.13$, we take some different Fr to display particle motion features. When $Fr^2=4.5\times10^3, 5.6\times10^2, 70.3$, and 8.8, the particles remain at the cores of vortices as drawn in Figure 5(a), which is similar to the phenomenon described in Figure 3(a). However, when $Fr^2=1.1$ in Figure 5(b) and 0.56 in Figure 5(c), the particle motion has different features described in Figure 3(a). Many particles move from the upper level vortices in the vortex street to the lower level ones. At the same time, the particles move from the cores of vortices to outside of the cores and the edge of vortex street. When $Fr^2=0.41, 0.24$ and 0.14, all particles concentrate in the lower-level vortices and the lower edge of the vortex street as drawn in Figure 5(d). As downstream

DOI: 10.1002/fld

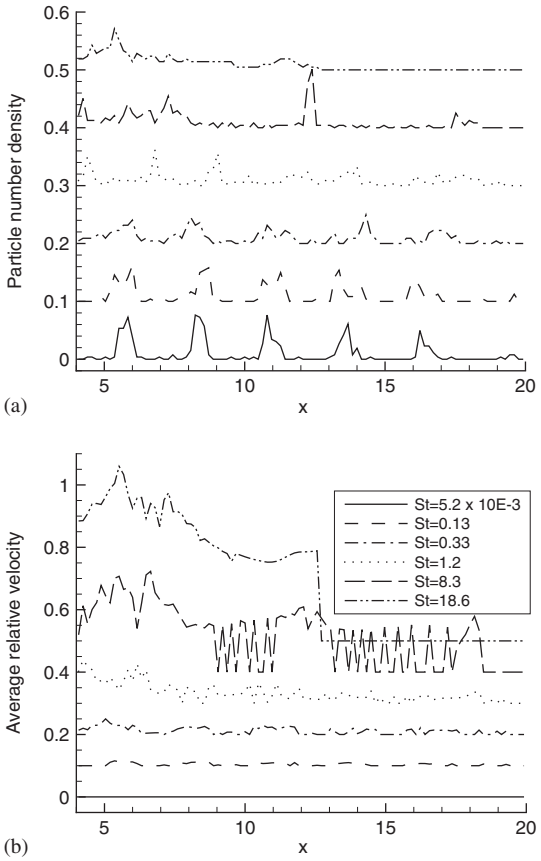

Figure 4. (a) Particle number density $\rho^m_{x_i+\Delta x/2}$ and (b) average relative velocity $v^m_{x_i+\Delta x/2}$ versus the streamwise distance for the intermediate and far wake field. The correspondent physical coefficients given in Figure 3(a)–(f) have a fixed $Fr^2=70.3$ and different St, which are shown in Figure 4(b) and denoted by solid, dash, dash-dot, dot, long dash and dash-dot-dot lines, respectively. For each St, an integral multiple of 0.1 is added to both $\rho^m_{x_i+\Delta x/2}$ and $v^m_{x_i+\Delta x/2}$, so that the correspondent lines can be in sight.

distance increases, the particles escape from the vortex street central region. We also investigate the particle motion features at fixed $St=4.7\times10^{-2}$ and 2.1, the global phenomena are similar to those described above, but have different thresholds for Fr.

In Equation (7), both St and Fr govern the transverse velocity V_y of particles and present coefficients of viscous force and gravity terms, respectively. In order to display the effects of Fr on the particle motion, we introduce a parameter

$$\kappa=(Fr^2)^{-1}/St^{-1}=St/Fr^2=\frac{gd_p^2}{18\varepsilon\nu_f U_\infty}=\frac{gT}{U_\infty}\approx\frac{u_T}{U_\infty} \tag{20}$$

where $u_T=gd_p^2\delta/18\nu_f$ is the gravitational settling velocity. κ presents a ratio of the particle transverse velocity under the acceleration of gravity in the particle relaxation time to the characteristic

DOI: 10.1002/fld

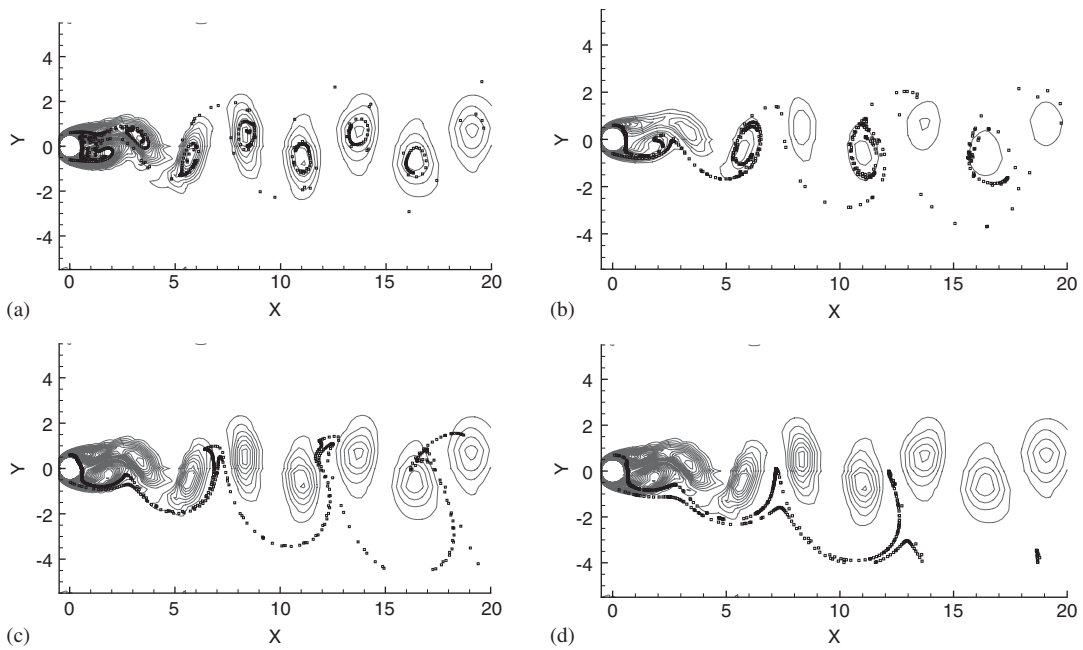

Figure 5. Instantaneous solid particle distribution and vorticity counter plot in the plane wake flow with a different Froude and a fixed $St=0.13$: (a) $Fr^2=70.3$ ($\kappa=1.8\times10^{-3}$); (b) $Fr^2=1.1$ ($\kappa=0.12$); (c) $Fr^2=0.56$ ($\kappa=0.23$); and (d) $Fr^2=0.41$ ($\kappa=0.32$).

velocity of wake flow. The particle transverse velocity equals approximately to the gravitational settling velocity. When $\kappa\leqslant0.05$, the particle motion patterns only depend on St and the main distribution of particles is in the vortex street central region. The Stokes drag term is a major term in Equation (7) and the gravity term can be neglected. When $0.05<\kappa\leqslant0.25$, the particles concentrate in the vortex street lower region and have only a few of the particles in the vortex street upper region. The gravity term is a major term in Equation (7), but the Stokes term cannot be neglected. When $0.25<\kappa$, the particles escape from the vortex street central region as downstream distance increases. The Stokes term in Equation (7) can be neglected. As the particle motion features change continuously, the thresholds 0.05 and 0.25 are only approximate ones. However, they can still provide a qualitative criterion for Fr.

(2) *For hollow sphere*: In Equation (8), the fluid stress term, the viscous drag term and the lift force term increase as ξ or equivalent particle density $\rho_p/(1-\xi^3)$ increases. Their orders are approachable; hence, we choose the viscous drag term in Equation (8) and compare with the gravity term to classify particle motion patterns . For a given ξ, Fr is fixed, particle motion patterns for the hollow sphere evaluated with St, i.e. d_p are similar to those for the solid sphere. So we only consider changes of ξ for a fixed $d_p=7\times10^{-5}$ m.

First, we choose U_∞ as 1 m/s to get $Fr^2=70.3$. ξ is changed from 0 to 0.999 and some basic features of particle trajectories are drawn in Figure 6. In order to check thresholds of κ, we also give its values in the caption of Figure 6. When $\xi=0$ ($St=25.4$), the sphere is solid, the particles escape from the vortex street central region as drawn in Figure 6(a). When $\xi=0.3$ ($St=24.7$), the

DOI: 10.1002/fld

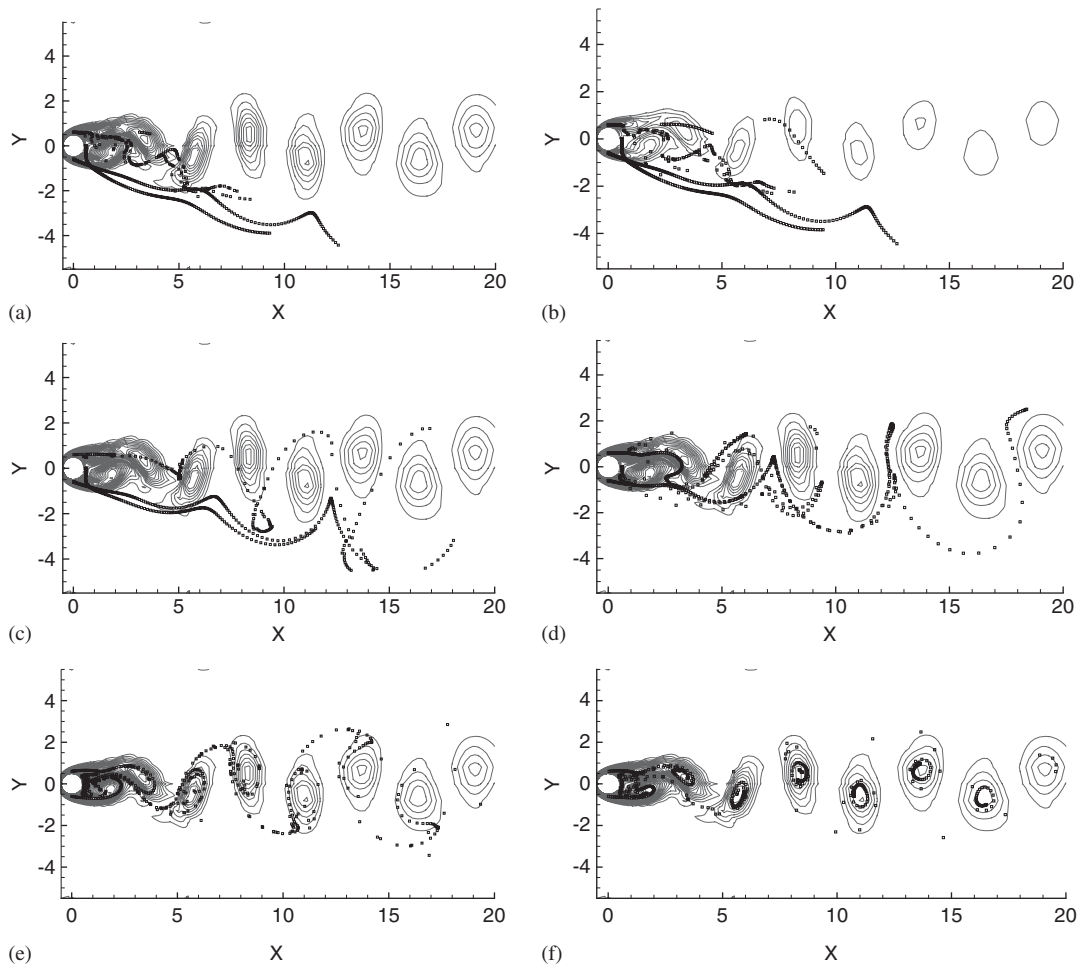

Figure 6. Instantaneous hollow particle distribution and vorticity counter plot in the plane wake flow with a different ratio ξ of inner diameter of particle to outer diameter and a fixed $Fr^2=70.3$: (a) $\xi=0$ ($St=25.4$ and $\kappa=0.36$); (b) $\xi=0.3$ ($St=24.7$ and $\kappa=0.35$); (c) $\xi=0.7$ ($St=16.7$ and $\kappa=0.24$); (d) $\xi=0.9$ ($St=6.9$ and $\kappa=0.10$); (e) $\xi=0.99$ ($St=0.76$ and $\kappa=1.7\times10^{-2}$); and (f) $\xi=0.999$ ($St=0.08$ and $\kappa=1.0\times10^{-3}$).

particle motion patterns in Figure 6(b) are similar to those in Figure 6(a). When $\xi=0.7$ ($St=16.7$), the particles, which concentrate at the edge of vortex street, have a main distribution in the lower region as drawn in Figure 6(c). When $\xi=0.9$ ($St=6.9$), the particle motion patterns in Figure 6(d) are similar to those in Figure 6(c). When $\xi=0.99$ ($St=0.76$), the particles concentrate at the edge of vortex street as drawn in Figure 6(e). When $\xi=0.999$ ($St=0.08$), the particles mainly fill the cores of vortices as drawn in Figure 6(f). Hence, the evolution of hollow particle motion patterns for the increase of ξ or $\rho_p/(1-\xi^3)$ corresponds to that of solid particle motion patterns for the decrease of d_p.

The above basic features of particle trajectories can be quantitatively represented by the particle number density and average relative velocity. For large enough St ($St=25.4, 24.7, 16.7$ and 6.9),

DOI: 10.1002/fld

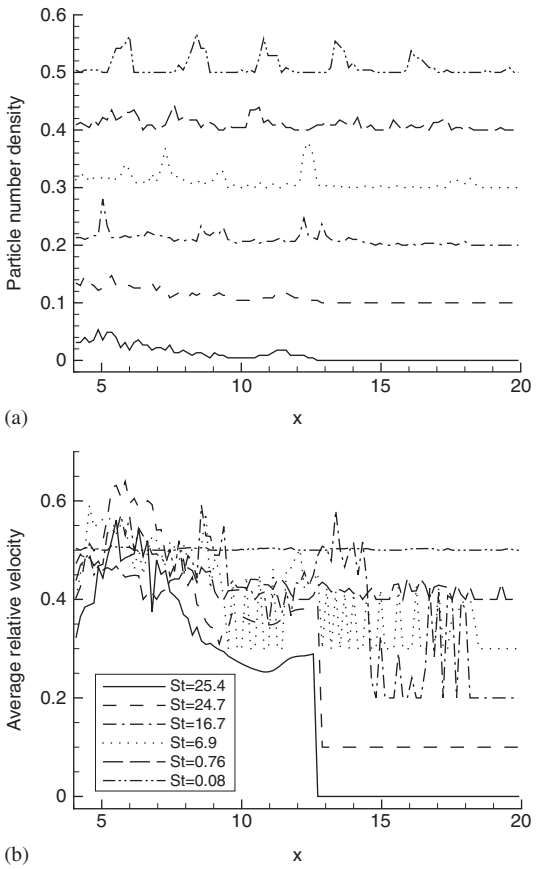

Figure 7. (a) particle number density $\rho^m_{x_i+\Delta x/2}$ and (b) average relative velocity $v^m_{x_i+\Delta x/2}$ versus the streamwise distance for the intermediate and far wake field. The correspondent physical coefficients given in Figure 6(a)–(f) have a fixed $Fr^2=70.3$ and different St, which are shown in Figure 7(b) and denoted by solid, dash, dash-dot, dot, long dash and dash-dot-dot lines, respectively. For each St, respectively. For each St, an integral multiple of 0.1 is added to both $\rho^m_{x_i+\Delta x/2}$ and $v^m_{x_i+\Delta x/2}$, so that the correspondent lines can be in sight.

in Figure 7(a), $\rho^m_{x_i+\Delta x/2}$ has only finite values in the intermediate wake field, but has not regular characters. In Figure 7(b), $v^m_{x_i+\Delta x/2}$ has very large values. It is shown that the hollow particle motion deviates seriously from the fluid element one on both positions and velocities. For the lower $St=0.76$, $\rho^m_{x_i+\Delta x/2}$ has only several high values with a constant downstream distance in the intermediate wake field, but has not in the far wake field. Meanwhile, $v^m_{x_i+\Delta x/2}$ has also finite values. It is shown that the hollow particle velocities deviate from the fluid element ones. So, the hollow particles may display the features of vortices in the intermediate wake, but have different velocities from fluid elements. For the lowest $St=0.08$, $\rho^m_{x_i+\Delta x/2}$ has several high values with the constant distance. The constant distance presents the streamwise one between two nearby vortices in the von Kármán vortex street. $v^m_{x_i+\Delta x/2}$ is almost zero in the intermediate and far wake field.

DOI: 10.1002/fld

It is shown that the hollow particle motion displays the fluid element one on both positions and velocities.

Second, we take U_∞ as 0.5 m/s to get $Fr^2 = 8.8$. The evolution of particle motion patterns is very similar to that for $Fr^2 = 70.3$. The gravitational term in Equation (8) increases as Fr decreases, so that many of the particles escape from the vortex street central region. However, to compare with the case for $Fr^2 = 70.3$, St decreases when ξ increases from 0 to 0.999. The viscous drag term increases that can reduce the effect of gravity term on particle motion.

It is clear that the particle motion patterns depend on both St and Fr. When κ is introduced, the evolution of patterns for the hollow sphere conforms with the qualitative criterion for the solid sphere. Although the thresholds have a little moving from 0.05 and 0.25, κ can still provide a good qualitative classification for the particle motion patterns during the changes of ξ or $\rho_p/(1-\xi^3)$.

5. CONCLUSION AND DISCUSSIONS

In this paper, dilute particle dynamics in a plane wake flow at a moderate Reynolds number is studied by using the spectral element method. With an instantaneous wake flow field, particle dynamics equations are solved to make a detail classification of the patterns in relation to the Stokes and Froude numbers. It is found that particle motion features only depend on the Stokes number at a high Froude number and depend on both numbers at a low Froude number. A ratio κ of the Stokes number to squared Froude number is proposed to make thresholds of the different effects on the particle motion. When $\kappa \leqslant 0.05$, the particle motion patterns only depend on the Stokes number and the main distribution of particles is in the vortex street central region. When $0.05 < \kappa \leqslant 0.25$, the particles concentrate in the vortex street lower region and has only a few of the particles in the vortex street upper region. When $0.25 < \kappa$, the particles escape from the vortex street central region as the downstream distance increases. The parameter describes approximately the gravitational settling velocity divided by the characteristic velocity of wake flow. In order to present effects of particle density but preserve rigid sphere, hollow sphere particle dynamics in the plane wake flow is investigated. The evolution of hollow particle motion patterns for the increase of equivalent particle density corresponds to that of solid particle motion patterns for the decrease particle size. Although the thresholds change a little, the parameter can still make a good qualitative classification of particle motion patterns as the inner diameter changes.

We emphasize that the current research is to develop the numerical method for particle motion at a moderate Reynolds number and the above result for the thresholds pertains to the special $Re = 100$. Whether the dependence of the thresholds on Re is simple remains to be determined. Moreover, for our investigation of particle interaction with vortices, a practical application is to provide some criteria of particle distribution patterns for particle image velocimetry technique.

ACKNOWLEDGEMENTS

The author thanks the referee for valuable suggestions and IMECH/ICTS research computing facilities for assisting in the computation.

DOI: 10.1002/fld

REFERENCES

1. Hunt JCR. Industrial and environmental fluid mechanics. *Annual Reviews of Fluid Mechanics* 1991; **23**:1–41.
2. Crowe CT, Chung JN, Troutt TR. Particle dispersion by organized turbulent structures. In *Particulate Two-phase Flow*, Roco MC (ed.). Butterworth-Heinemann: London, 1993; 626–669.
3. Maxey MR, Riley JJ. Equation of motion for a small rigid sphere in a nonuniform flow. *Physics of Fluids* 1983; **26**:883–889.
4. Auton TR, Hunt JCR, Prud'homm M. The force exerted on a body in an inviscid unsteady non-uniform rotation flow. *Journal of Fluid Mechanics* 1988; **197**:241–257.
5. Maxey MR. The motion of small spherical particles in a cellular flow field. *Physics of Fluids* 1987; **30**:1915–1928.
6. Tio KK, Ganan-Calvo AM, Lasheras JC. The dynamics of small, heavy, rigid spherical particles in a periodic Stuart vortex flow. *Physics of Fluids* 1993; **5**:1679–1693.
7. Wu ZB, Ling GC, Xing QJ. Effects of particle size on dilute particle dispersion in a Karman vortex street flow. *Chinese Physics Letters* 2002; **19**:83–86.
8. Wu ZB. Streamline topology and dilute particle dynamics in a Karman vortex street flow. *International Journal of Bifurcation and Chaos* 2003; **13**:1275–1286.
9. Crowe CT, Chung JN, Troutt TR. Particle interaction with vortices. In *Fluid Vortices*, Green SI (ed.). Kluwer Academic Publishers: Dordrecht, 1995; 829–858.
10. Wen F, Kamalu N, Chung JN, Crowe CT, Troutt TR. Particle dispersion by vortex structures in plane mixing layers. *Journal of Fluids Engineering* 1992; **114**:657–666.
11. Tang L, Wen F, Yang Y, Crowe CT, Chung JN, Troutt TR. Self-organizing particle dispersion mechanism in a plane wake. *Physics of Fluids* 1992; **4**:2244–2251.
12. Yang Y, Crowe CT, Chung JN, Troutt TR. Experiments on particle dispersion in a plane wake. *International Journal of Multiphase Flow* 2000; **26**:1583–1607.
13. Karniadakis GE, Israeli M, Orszag SA. High-order splitting methods for the incompressible Navier–Stokes equations. *Journal of Computational Physics* 1991; **97**:414–443.
14. Patera AT. A spectral element method for fluid dynamics: laminar flow in a channel expansion. *Journal of Computational Physics* 1984; **54**:468–488.
15. Korczak KZ, Patera AT. An isoparametric spectral element method for solution of the Navier–Stokes equations in complex geometry. *Journal of Computational Physics* 1986; **62**:361–382.
16. Karniadakis GE, Sherwin SJ. *Spectral/hp Element Methods for CFD*. Oxford University Press: New York, 1999.
17. Karniadakis GE, Triantafyllou GS. Three-dimensional dynamics and transition to turbulence in the wake of bluff objects. *Journal of Fluid Mechanics* 1992; **238**:1–30.
18. Henderson RD. Nonlinear dynamics and pattern formation in turbulent wake transition. *Journal of Fluid Mechanics* 1997; **352**:65–112.
19. Clift R, Grace JR, Weber ME. *Bubbles, Drops and Particles*. Academic Press: New York, 1978.
20. Zang TA. On the rotation and skew-symmetric forms for incompressible flow simulations. *Applied Numerical Mathematics* 1991; **7**:27–40.
21. Panton RL. *Incompressible Flow*. Wiley: New York, 1984.
22. Gordon WJ, Hall CA. Construction of curvilinear co-ordinate systems and their applications to mesh generation. *International Journal for Numerical Methods in Engineering* 1973; **7**:461–477.
23. Gordon WJ, Hall CA. Transfinite element methods: blending-function interpolation over arbitrary curved element domains. *Numerische Mathematik* 1973; **21**:109–129.
24. Hageman LA, Young DM. *Applied Iterative Methods*. Academic Press: New York, 1981.
25. Press WH, Teukolsky SA, Vetterling WT, Flannery BP. *Numerical Recipes in C* (2nd edn). Cambridge University Press: London, 1992.
26. Barkley D, Henderson RD. Three-dimensional Floquest stability analysis of the wake of a circular cylinder. *Journal of Fluid Mechanics* 1996; **322**:215–241.
27. Zhang HQ, Fey U, Noack BR. On the transition of the cylinder wake. *Physics of Fluids* 1995; **7**:779–794.
28. Henderson RD. Details of the drag curve near the onset of vortex shedding. *Physics of Fluids* 1995; **7**:2102–2104.

DOI: 10.1002/fld